THE JOURNAL OF BIOLOGICAL CHEMISTRY VOL. 290, NO. 5, pp. 2946–2956, January 30, 2015
Published in the U.S.A.

Structural and Inhibitory Effects of Hinge Loop Mutagenesis in Serpin-2 from the Malaria Vector *Anopheles gambiae*[*]

Received for publication, November 14, 2014, and in revised form, December 10, 2014 Published, JBC Papers in Press, December 17, 2014, DOI 10.1074/jbc.M114.625665

Xin Zhang[‡1], David A. Meekins[‡1], Chunju An[‡§], Michal Zolkiewski[¶], Kevin P. Battaile[‖], Michael R. Kanost[¶], Scott Lovell[**], and Kristin Michel[‡2]

*From the [‡]Division of Biology, Kansas State University, Manhattan, Kansas 66506, the [§]Department of Entomology, College of Agriculture and Biotechnology, China Agricultural University, Beijing, China, the [¶]Department of Biochemistry and Molecular Biophysics, Kansas State University, Manhattan, Kansas 66506, [‖]Industrial Macromolecular Crystallography Association Collaborative Access Team, Hauptman-Woodward Medical Research Institute, Advanced Photon Source Argonne National Laboratory, Argonne, Illinois 60439, and the **Protein Structure Laboratory, Del Shankel Structural Biology Center, University of Kansas, Lawrence, Kansas 66407*

Background: Serpin-2 (SRPN2) is a key regulator of mosquito immunity and contains an inserted hinge region linked to activation in other serpins.
Results: Structure/function analyses of hinge mutations refute a hypothesized activation mechanism in SRPN2.
Conclusion: SRPN2 hinge insertion provides a thermodynamically stable conformation without restricting inhibitory capability.
Significance: To effectively utilize SRPN2 for vector control, its mode of action must be understood.

Serpin-2 (SRPN2) is a key negative regulator of the melanization response in the malaria vector *Anopheles gambiae*. SRPN2 irreversibly inhibits clip domain serine proteinase 9 (CLIPB9), which functions in a serine proteinase cascade culminating in the activation of prophenoloxidase and melanization. Silencing of SRPN2 in *A. gambiae* results in spontaneous melanization and decreased life span and is therefore a promising target for vector control. The previously determined structure of SRPN2 revealed a partial insertion of the hinge region of the reactive center loop (RCL) into β sheet A. This partial hinge insertion participates in heparin-linked activation in other serpins, notably antithrombin III. SRPN2 does not contain a heparin binding site, and any possible mechanistic function of the hinge insertion was previously unknown. To investigate the function of the SRPN2 hinge insertion, we developed three SRPN2 variants in which the hinge regions are either constitutively expelled or inserted and analyzed their structure, thermostability, and inhibitory activity. We determined that constitutive hinge expulsion resulted in a 2.7-fold increase in the rate of $CLIPB9_{Xa}$ inhibition, which is significantly lower than previous observations of allosteric serpin activation. Furthermore, we determined that stable insertion of the hinge region did not appreciably decrease the accessibility of the RCL to CLIPB9. Together, these results indicate that the partial hinge insertion in SRPN2 does not participate in the allosteric activation observed in other serpins and instead represents a molecular trade-off between RCL accessibility and efficient formation of an inhibitory complex with the cognate proteinase.

Anopheles gambiae mosquitoes are dominant insect vectors for the most virulent species of human malaria parasites, *Plasmodium falciparum*, in Africa (1–3). Malaria continues to be a devastating disease, responsible for over 800,000 deaths in 2013, mostly among children in sub-Saharan Africa (4). The lack of vaccines and substandard medical resources in infected areas, coupled with drug resistance, complicate successful treatment of infected patients (5, 6). Vector control remains the foremost method for controlling the spread of malaria, but resistance to all four classes of insecticides has been reported in malaria vectors (4, 7, 8). This highlights the need for new insecticides that are less susceptible to the selective pressures that drive resistance. Theoretical studies have suggested that late life-acting insecticides that target females would be the most effective measure to impact vector populations without facilitating resistance (9, 10). The serine proteinase inhibitor SRPN2[3] is a particularly promising potential late life-acting insecticide target in *A. gambiae* (11, 12). SRPN2 is a negative regulator of the mosquito melanization response, and depletion of SRPN2 in *A. gambiae* causes spontaneous melanization and significantly shortens the life span of adult female mosquitoes (11). Chemically targeting SRPN2 in field mosquito popula-

* This work was supported, in whole or in part, by National Institutes of Health Grant R01AI095842 (to K. M.). Use of the University of Kansas Protein Structure Laboratory was supported by National Institutes of Health Grants 5P20RR017708-10 and 8P20GM103420-10. Use of the Industrial Macromolecular Crystallography Association Collaborative Access Team beamline 17-ID at the Advanced Photon Source was supported by the companies of the Industrial Macromolecular Crystallography Association through a contract with Hauptman-Woodward Medical Research Institute. Use of the Advanced Photon Source was supported by the United States Department of Energy, Office of Science, Office of Basic Energy Sciences, under Contract DE-AC02-06CH11357.

The atomic coordinates and structure factors (codes 4RO9, 4ROA, and 4RSQ) have been deposited in the Protein Data Bank (http://wwpdb.org/).

[1] Both authors contributed equally to this work.

[2] To whom correspondence should be addressed: Kansas State University, Division of Biology, 267 Chalmers Hall, Manhattan, KS 66506. Tel.: 785-532-0161; Fax: 785-532-6653; E-mail: kmichel@ksu.edu.

[3] The abbreviations used are: SRPN, serpin; CLIPB, clip domain serine proteinase; RCL, reactive center loop; ATIII, antithrombin III; H5, heparin pentasaccharide; SI, stoichiometry of inhibition; Bistris propane, 1,3-bis[tris-(hydroxymethyl)methylamino]propane.

tions therefore shows promise in limiting the spread of malaria in endemic areas.

SRPN2 is part of a complex regulatory pathway that modulates the insect immune response (13–15). Insects lack an adaptive immune system and must rely solely upon innate immune reactions, including melanization, to combat infectious organisms (14). Melanization is employed to encapsulate and kill invading pathogens and is initiated upon pathogen detection (16). Recognition proteins in the insect hemolymph recognize non-self biomolecules and activate a clip domain serine proteinase cascade (17–20). This cascade culminates in the activation of prophenoloxidase-activating proteinases, which convert prophenoloxidase to phenoloxidase (21–23). Phenoloxidase hydroxylates monophenols to catechols and oxidizes catechols to quinones, which polymerize to form eumelanin (24, 25). Although melanization is an efficient mechanism for targeting foreign pathogens, it adversely affects insect longevity (11). Uncontrolled melanization is likely to be physiologically detrimental due to the production of reactive and toxic byproducts (16) and, thus, the probable cause of the decreased life span of SRPN2-depleted mosquitoes.

The specific SRPNs and cognate functional clip domain serine proteinases (CLIPBs) that interact to regulate the melanotic response in *A. gambiae* are still largely uncharacterized (26). However, SRPN2 inhibits CLIPB9 both *in vitro* and *in vivo* and is the most well characterized regulatory interaction in the mosquito melanization pathway (12). CLIPB9 contains a single N-terminal clip domain and a C-terminal serine proteinase catalytic domain and is synthesized as a zymogen, becoming activated upon proteolytic cleavage at the beginning of the catalytic domain (12). Serpins inhibit proteinases via a suicide inhibitory mechanism that results in permanent inactivation of both the serpin and its cognate proteinase (27, 28). Serpins generally contain 350–400 amino acids and adopt a conserved native fold consisting of three β-sheets (A, B, and C) surrounded by up to nine α-helices (A–I) with a reactive center loop (RCL) that acts as bait for target proteinases. This native serpin fold exists in a stressed, metastable form. Upon cleavage of the RCL scissile bond (P1-P1′) by a target proteinase, the acyl-intermediate undergoes a remarkable 70-Å translocation whereby the RCL is inserted into β-sheet A as an additional β-strand (29). This conformational change is achieved because the relaxed, cleaved form is more thermodynamically stable than the native fold. The translocation disrupts the integrity of the proteinase active site, rendering it inactive and covalently linked to the serpin in an SDS-stable complex (30). SRPN2 uses this mechanism to permanently inactivate CLIPB9, thereby limiting phenoloxidase activation and the melanotic immune response (12).

The crystal structure of *A. gambiae* SRPN2 was previously determined to a resolution of 1.75 Å in its native, active form (31). As expected, SRPN2 adopts the conserved serpin fold. The most notable difference between SRPN2 and most other native serpins is the conformation of the N-terminal region of the RCL, the hinge region, composed of residues Leu^{356}–Ala^{360}. The SRPN2 hinge region is partially inserted between strands 3 and 5 of β-sheet A (βA3 and βA5). A similar partial hinge insertion has only been found in a small number of inhibitory serpins: non-heparin-bound antithrombin III (ATIII) (32, 33), heparin cofactor II (34), murine antichymotrypsin (35), and Spn48 from *Tenebrio molitor* (36). In ATIII, the partial hinge insertion is linked to heparin-mediated activation. This insertion in ATIII restricts the flexibility of the RCL, which limits accessibility of the P1-P1′ bond to the target proteinase (37–39). Binding of heparin pentasaccharide (H5) to helix D induces significant conformational changes, including C-terminal helix D extension and expulsion of the hinge region, resulting in extension of the RCL. As a result of these conformational changes, ATIII activity dramatically increases against factors IXa and Xa (34, 37, 40, 41). Further evidence for H5-mediated activation of a hinge-inserted serpin is reported for Spn48, in which heparin binding significantly increases inhibition against its target proteinase (36). However, SRPN2 does not contain a heparin binding site, and H5 does not increase the activity of SRPN2 against $CLIPB9_{Xa}$ (31). Therefore, although SRPN2 contains a partial hinge insertion linked to allosteric inactivation of some other serpins, its mechanistic role in SRPN2, if any, is entirely unknown.

In previous studies, mutagenesis was employed to either constitutively expel or stabilize the hinge insertion of ATIII to determine the concomitant effect on inhibitory activity (40, 42–44). Mutation-induced expulsion of the hinge region mimicked heparin activation in ATIII, and mutation-induced restriction of the hinge region significantly diminished its inhibitory capability (42, 44). In the current study, we used equivalent mutations in SRPN2 to elucidate the influence of the partial hinge insertion on SRPN2 inhibition of $CLIPB9_{Xa}$. We created SRPN2 mutations that constitutively expelled (S358E) or restricted (S358W, E359C/K198C) the hinge region, investigated the structural and thermodynamic effects of these mutations, and determined the mutants' ability to inhibit $CLIPB9_{Xa}$. The results indicate that the partial hinge insertion in SRPN2 is not a structural regulatory mechanism as observed in ATIII. Instead, the data suggest that the partial hinge insertion in SRPN2 is thermodynamically stable, permits P1-P1′ accessibility to $CLIPB9_{Xa}$, and maintains the ability to efficiently form inhibitory complexes.

EXPERIMENTAL PROCEDURES

Cloning, Expression, and Purification of Recombinant Proteins—A. gambiae SRPN2-WT was cloned previously into a pET-28a vector to encode the full-length mature protein and an N-terminal His_6 tag (12). *A. gambiae* SRPN2-S358W was generated using the QuikChange multisite-directed mutagenesis kit (Stratagene) following the manufacturer's instructions. The following mutagenic primer was used to mutate Ser^{358} to a tryptophan: 5′-ATCACCATCAATGAGCTGGGCTGGGAGGCTTACGCTGCTACCGA-3′. *A. gambiae* SRPN2-S358E was generated by a site-directed, ligase-independent mutagenesis method as described previously (75). The following mutagenic primers were used to mutate Ser^{358} to a glutamate: Ft, 5′-GGGCGAGGAGGCTTACGCTGCTACCGAAATTCAACTCG-3′; Fs, 5′-TGCTACCGAAATTCAACTCG-3′; Rt, 5′-GCGTAAGCCTCCTCGCCCAGCTCATTGATGGTGATGCC-3′; Rs, 5′-AGCTCATTGATGGTGATGCC-3′. *A. gambiae* SRPN2-K198C/E359C was generated using the QuikChange multisite-directed mutagenesis kit (Stratagene) to first

generate the K198C mutation with the mutagenic primer 5′-CTGGTCAATGTTATCTACTTCTGTGGCCTGTGGACG-TACCCGTTC-3′, followed by generation of the E359C mutation using the site-directed, ligase-independent mutagenesis method with the primers Ft (5′-GGGCAGTTGCGCTTACG-CTGCTACCGAAATTCAACTCG-3′), Fs (5′-TGCTACCGA-AATTCAACTCG-3′), Rt (5′-GCGTAAGCGCAACTGCCCA-GCTCATTGATGGTGATGCC-3′), and Rs (5′-AGCTCATTG-ATGGTGATGCC-3′). All mutagenesis was confirmed by DNA sequencing (Genewiz).

All SRPN2 variant proteins were expressed and purified as described previously with the following modifications (12, 45). The plasmid constructs were used to transform *Escherichia coli* strain BL21(DE3) competent cells (Invitrogen). Bacteria were grown in 1 liter of LB medium at 37 °C until an A_{600} of 0.6–0.8 was reached. 0.1 mM isopropyl β-D-1-thiogalactopyranoside was then added, and the cells were shaken at 20 °C and 150 rpm for 16 h. The cells were then lysed by sonication and purified by nitrilotriacetic acid-agarose chromatography (Qiagen), followed by ion exchange chromatography on a Q-Sepharose column (GE Healthcare). The fractions were examined by 10% SDS-PAGE and Coomassie Blue staining to confirm homogeneity. Fractions containing sufficiently pure recombinant protein were pooled for later use.

The cloning, expression, and purification of recombinant *A. gambiae* proCLIPB9$_{Xa}$ were performed as described previously with the following modifications. Full-length *A. gambiae* proCLIPB9 was cloned into a pFastBac1 (Invitrogen) vector, and the activation cleavage site (IGMR) was mutated (IEGR) via a QuikChange multisite-directed mutagenesis kit (Stratagene) to generate *A. gambiae* proCLIPB9Xa and permit controlled activation by factor Xa. Recombinant baculoviruses were generated by using the resulting plasmid according to the manufacturer's instructions (Invitrogen). Recombinant protein was expressed in Sf9 cells following the manufacturer's protocol and purified by nitrilotriacetic acid-agarose chromatography (Qiagen) followed by ion exchange chromatography on a Q-Sepharose column (GE Healthcare). The fractions were examined by 10% SDS-PAGE and Coomassie Blue staining to confirm homogeneity. Fractions containing sufficiently pure recombinant protein were pooled for later use.

Determination of SRPN2 Mutant Crystal Structures—All crystallization screening was conducted in Compact Jr. (Rigaku Reagents) sitting drop vapor diffusion plates at 20 °C using equal volumes or protein and crystallization solution equilibrated against 75 μl of the latter. Protein samples were concentrated to 15.5 mg/ml (SRPN2-S358E), 12.1 mg/ml (SRPN2-S358W), and 9.8 mg/ml (SRPN2-K198C/E359C) in 150 mM NaCl, 20 mM Tris, pH 8.0. Prismatic crystals of SRPN2-S358E were obtained in 1–2 days from the Wizard 3–4 screen (Rigaku Reagents) condition G6 (20% (w/v) PEG 3350, 100 mM Bistris propane, pH 8.5, and 200 mM sodium malonate). SRPN2-S358W crystals displaying a prismatic morphology were obtained in 1–2 days from the Index HT screen (Hampton Research) condition C5 (60% (w/v) Tacsimate, pH 7.0). SRPN2-K198C/E359C grew as plate crystals in 2 days from the SaltRx HT screen (Hampton Research) condition E6 (1.0 M sodium phosphate monobasic monohydrate, potassium phosphate dibasic, pH 6.9). All sample crystals were transferred to a solution containing 80% crystallization solution and 20% glycerol as a cryoprotectant before freezing in liquid nitrogen except for SRPN2-K198C/E359C crystals, which utilized a cryoprotectant of 70% crystallization solution and 30% glycerol. X-ray diffraction data were collected at the Advanced Photon Source Industrial Macromolecular Crystallography Association Collaborative Access Team beamline 17-ID using a Dectris Pilatus 6M pixel array detector.

Intensities were integrated using XDS (46), and the Laue class check and data scaling were performed with Aimless (47). Structure solution was conducted by molecular replacement with Phaser (48) via the Phenix (49) or Molrep (50) interface using the SRPN2-WT structure (PDB entry 3PZF) (31) as the search model. Refinement and manual model building were carried out with Phenix and Coot (51), respectively. TLS (transition/liberation/screw) refinement (52) was incorporated in the later stages to model anisotropic atomic displacement parameters. Structure validation was conducted with Molprobity (53). Disordered side chains were truncated to the point where electron density could be observed. Figures were prepared using PyMOL (54) and the CCP4MG package (55). Relevant crystallographic data are provided in Table 1. The structures were deposited in the Protein Data Bank with the following accession numbers: SRPN2-S358E (4RO9), SRPN2-S358W (4ROA), and SRPN2-K198C/E359C (4RSQ).

The diffraction data for SRPN2-K198C/E359C were initially indexed in an orthorhombic *P* lattice ($a = 97$, $b = 164$, $c = 186.23$) and displayed a large pseudotranslation peak of ~30% of the origin at 0.263, 0.5, 0.456, and the self-rotation function indicated 3-fold non-crystallographic symmetry parallel to the crystallographic *b* axis. The two non-crystallographic symmetry trimers were positioned by molecular replacement with Phaser and Molrep using a single chain from PDB entry 3PZF as the search model. The same solutions were obtained with both programs with the top score in the space group *P*222. However, following refinement, the electron density was clear for one trimer (chains A–C) but poor for the second trimer (chains D–F), and the *R*-factors converged at $R/R_{free} = 29\%/36\%$. The molecules were arranged in rows that stacked along the crystallographic *b* axis and consisted of alternating sets of two A–C trimer rows and two D–F trimer rows. Inspection of the crystal packing revealed that chain D of the D–F trimer overlapped a symmetry mate related by a crystallographic 2-fold axis along *b*. We considered that this might be a case of lattice translocation disorder given that the diffraction spots were streaked along the *b** reciprocal lattice direction. However, this condition is typified by alternating strong and diffuse spots in the diffraction pattern (56), which was not observed for the SRPN2-K198C/E359C crystals. The data were reprocessed in a *P*1 unit cell, and a molecular replacement solution consisting of 24 molecules (8 trimers) was obtained with Molrep. This allowed us to determine the packing arrangement of the trimers and subsequently apply the results of this solution to a higher symmetry monoclinic *P* lattice ($P2_1$, $a = 97.93$, $b = 164.39$, $c = 186.18$, $\beta = 90.04°$) containing 12 molecules (4 trimers) in the asymmetric unit. Further confirmation was obtained with the program Zanuda (57), which yielded the same top solution for the mono-

clinic $P2_1$ lattice. Twin refinement with Refmac (58) using the pseudomerohedral twin law ($h, -k, -l$), determined by Xtriage within the Phenix package, yielded a final model with R/R_{free} = 19.4/25.5% and a twin fraction of 45%. Thus, it appeared that the crystal structure was best modeled as a monoclinic *P* lattice with a β-angle near 90°, which "mimicked" a higher symmetry orthorhombic *P* lattice.

Reducing/Nonreducing SDS-PAGE Analysis—To analyze the presence of a disulfide bond in SRPN2-K198C/E359C, proteins were boiled at 95 °C for 10 min in SDS-PAGE loading buffer (50 mM Tris-HCl (pH 6.8), 2% SDS, 0.1% bromphenol blue, and 10% glycerol) with and without 100 mM dithiothreitol (DTT). SDS-PAGE was then performed and stained with Coomassie Blue.

Differential Scanning Calorimetry—To determine the thermal stability of the SRPN2 mutants, purified protein (0.5 mg/ml) was dialyzed in 10 mM sodium phosphate, pH 7.6, and 150 mM NaCl overnight, degassed, and loaded into a VP-DSC microcalorimeter (MicroCal Inc.). The temperature was scanned at 1 °C/min from 20 to 80 °C. Heat capacity (*Cp*) (kcal/mol/K) was plotted after subtraction of a blank experiment without protein. A second scan for each protein was performed but excluded from the final data due to aggregation. To compare T_m of each protein, the baseline *Cp* was normalized to SRPN2-WT.

Activation of proCLIPB9$_{Xa}$—The activation of proCLIPB9$_{Xa}$ was performed as described previously (12) with the following modifications. 5 μg of purified proCLIPB9$_{Xa}$ was incubated with 2 μg of commercial bovine factor Xa (New England Biolabs) in a total volume of 100 μl (20 mM Tris-HCl, pH 8.0, 100 mM NaCl, 2 mM $CaCl_2$) at 37 °C for 16 h. Cleavage of the zymogen was examined by Western blot using anti-His antibody. To examine the amidase activity, 2 μl of the above reaction were transferred to a 96-well flat bottomed microplate (Corning, Inc.), followed by the addition of 200 μl of 1,000 μM acetyl-IEAR-*p*-nitroanilide (BioWorld) in buffer (0.1 M Tris-HCl, pH 8.0, 0.1 M NaCl, 5 mM $CaCl_2$). Absorbance changes at 405 nm were monitored immediately in a microplate reader (Bio-Tek Instruments, Inc.) every 30 s for 20 min. One unit of amidase activity was defined as ΔA_{405}/min = 0.001. Amidase activity of the serine proteinase was defined as the activity of enzyme minus the activity of factor Xa alone.

Serpin Inhibition Assays—To examine the inhibitory effect of serpins on proteinase activity, 100 ng of activated CLIPB9$_{Xa}$ in a volume of 2 μl was incubated with 4 μl of recombinant SRPN2 proteins at different molar ratios with the addition of 1 μl of BSA (2 μg/μl) at 23 °C for 20 min. The reaction was then subjected to an amidase activity assay as described above. Substitution of recombinant serpin with 4 μl of buffer (20 mM Tris-HCl, pH 8.0,100 mM NaCl) was used to determine 100% enzyme activity. Residual amidase activity was plotted against the ratio of SRPN2 to activated CLIPB9$_{Xa}$, and the stoichiometry of inhibition (SI) was determined as the *x* intercept of the linear regression fit. All experiments were carried out with at least three independent replicates.

The second-order rate constant (k_a) of interactions between SRPN2-WT or SRPN2-S358E and CLIPB9$_{Xa}$ was determined under pseudo-first order conditions as described previously (59). A fixed amount of CLIPB9Xa (2.4 pmol) was mixed with different concentrations of recombinant SRPN2 in 1,000 μM IEAR-*p*-nitroanilide. The progress of product formation (*P*) at each concentration of SRPN2 was measured immediately as described above. For each combination of enzyme and inhibitor, a k_{obs} value was calculated by nonlinear regression using the following equation,

$$P = V/k_{obs} \times (1 - e^{-k_{obs}t}) \quad \text{(Eq. 1)}$$

where *P* represents the amount of product formation, *V* is initial velocity, *t* is time, and k_{obs} is reaction rate. The k_a was determined by plotting a series of k_{obs} against the respective SRPN2 concentration and measuring the slope of the linear regression fit.

The association rate constant for the interaction between CLIPB9$_{Xa}$ and *A. gambiae* SRPN2-S358W or *A. gambiae* SRPN2-K198C/E359C was determined by a discontinuous second order rate constant inhibition assay as described previously with the following modifications (60). Briefly, *A. gambiae* SRPN2-S358W or *A. gambiae* SRPN2-K198C/E359C was added to activated CLIPB9$_{Xa}$ at a molar ratio of 100:1 and incubated at room temperature for varying periods of time (*t*), including 0, 10, 20, 20, 40, 60, 80, 100, and 120 min. The residual amidase activity was measured at each time point (V_t) as described above. Initial enzyme activity (V_0) was measured by replacing SRPN2 protein in the reaction with the same volume of buffer. The slope was calculated by plotting a series of $\ln(V_t/V_0)$ values against the respective incubation time. The k_a was calculated by dividing this negative slope by the concentration of the SRPN2 variants.

Detection of inhibitory complexes between SRPN2-CLIPB9$_{Xa}$ was performed as described previously (12). Activated CLIPB9Xa was mixed with purified SRPN2 at a molar ratio of 1:6 and incubated at room temperature for 10 min. The reaction mixtures were separated by 10% SDS-PAGE and stained with Coomassie Blue.

RESULTS

Structure of SRPN2-S358E—The previously determined crystal structure of *A. gambiae* SRPN2-WT revealed a characteristic serpin fold consisting of three β-sheets (A, B, and C) flanked by nine α-helices (A–I) (31). The SRPN2-WT RCL hinge region (residues Leu^{356}–Ala^{360}) was inserted into β-sheet A between strands βA3 and βA5. P14 residue Ser^{358} is located at the apex of the loop involved in the hinge insertion. The corresponding P14 residue in ATIII (Ser^{380}) was also located in this position, and its mutation to a glutamate (ATIII-S380E) resulted in an expulsion of the hinge region. Importantly, ATIII-S380E inhibitory activity against factor Xa is increased nearly 200-fold, to a level comparable with wild-type ATIII upon H5 activation (32, 44). To investigate the consequences of the hinge region insertion for SRPN2 structure and activity, we mutated Ser^{358} to a glutamate (SRPN2-S358E) in an attempt to constitutively expel the residue from β-sheet A in the native serpin conformation.

The conformation of the hinge region in SRPN2-S358E was characterized from the crystal structure, determined to a resolution of 2.0 Å (Table 1 and Fig. 1*A*) and contained three molecules in the asymmetric unit (Fig. 1*B*). The three subunits are nearly identical except for the number of residues that could be

TABLE 1
Crystallographic data for SRPN2 mutant structures

	SRPN2-S358E	SRPN2-S358W	SRPN2-K198C/E359C
Data collection			
Unit-cell parameters (Å, degrees)	$a = 171.33$, $b = 42.26$, $c = 185.62$, $\beta = 116.9$	$a = 96.95$, $c = 78.57$	$a = 97.93$, $b = 164.39$, $c = 186.18$, $\beta = 90.02$
Space group	$I2$	$P6_3$	$P2_1$
Resolution (Å)	93.5-2.00 (2.04-2.00)[a]	48.47-1.90 (1.94-1.90)	48.94-2.90 (2.95-2.90)
Wavelength (Å)	1.0000	1.0000	1.0000
Temperature (K)	100	100	100
Observed reflections	268,964	309,621	441,482
Unique reflections	80,845	33,155	129,666
$\langle I/\sigma(I)\rangle$	13.8 (2.1)	18.4 (2.7)	7.9 (2.0)
Completeness (%)	99.7 (99.7)	100 (100)	99.5 (99.8)
Multiplicity	3.3 (3.5)	9.3 (8.9)	3.4 (3.3)
R_{merge} (%)[b]	4.6 (46.9)	7.9 (79.8)	13.5 (63.5)
R_{meas} (%)[c]	6.5 (67.4)	8.4 (84.7)	16.1 (76.3)
R_{pim} (%)[c]	3.5 (35.8)	2.7 (28.2)	8.6 (41.8)
$CC_{½}$[d]	0.999 (0.849)	0.999 (0.881)	0.990 (0.752)
Refinement			
No. of molecules/asymmetric unit	3	1	12
Resolution (Å)	38.18-2.00	39.29-1.90	47.82-2.90
Reflections (working/test)	76,752/4,050	31,401/1,671	123,334/6,285
R_{factor}/R_{free} (%)[e]	19.0/23.8	17.2/21.0	19.4/25.5
No. of atoms (protein/water)	8,324/249	2,872/107	33,765/0
Model quality			
Root mean square deviations			
Bond lengths (Å)	0.009	0.010	0.006
Bond angles (degrees)	1.150	0.951	1.080
Average B-factor (Å^2)			
All atoms	41.1	40.4	43.4
Protein	41.4	40.6	43.4
Water	38.7	36.4	
Coordinate error (Å)	0.22	0.19	0.24
Ramachandran plot			
Favored (%)	96.4	98.0	95.4
Allowed (%)	3.1	2.0	4.3

[a] Values in parenthesis are for the highest resolution shell.
[b] $R_{merge} = \Sigma_{hkl}\Sigma_i|I_i(hkl) - \langle I(hkl)\rangle|/\Sigma_{hkl}\Sigma_i I_i(hkl)$, where $I_i(hkl)$ is the intensity measured for the ith reflection, and $\langle I(hkl)\rangle$ is the average intensity of all reflections with indices hkl.
[c] R_{meas} = redundancy-independent (multiplicity-weighted) R_{merge} (47, 70). R_{pim} = precision-indicating (multiplicity-weighted) R_{merge} (71, 72).
[d] $CC_{½}$ is the correlation coefficient of the mean intensities between two random half-sets of data (73, 74).
[e] $R_{factor} = \Sigma_{hkl}||F_o(hkl)| - |F_c(hkl)||/\Sigma_{hkl}|F_o(hkl)|$; R_{free} is calculated in an identical manner using 5% of randomly selected reflections that were not included in the refinement.

traced in the RCL hinge region (Fig. 1*C*). Although most of the RCL was disordered in each subunit, the RCL in chain A could be traced to residue Ala^{360} (Leu^{356}–Ala^{360} were inserted in SRPN2-WT) (Fig. 1*D*). Therefore, the A-chain was used for all further analysis of the SRPN2-S358E structure.

The overall structure of SRPN2-S358E is very similar to the SRPN2-WT structure. Superposition of the two structures using secondary structure matching (61) yielded a root mean square deviation of 0.76 Å between Cα atoms of the 353 residues aligned (Fig. 2*A*). As predicted, the most notable difference between the wild type and SRPN2-S358E structures is the RCL hinge region (Fig. 2*B*). The SRPN2-S358E hinge region is indeed expelled from β-sheet A, translocated ~12 Å from the inserted position in SRPN2-WT. Glu^{358} forms hydrogen bonds with Lys^{47} in helix A of the A-chain of a symmetry-related molecule, Arg^{252} located between βB2 and βB3, and Lys^{114} located between helix D and βA1 (Fig. 2*C*). Overall, these structural data confirm that SRPN2-S358E assumes the native serpin fold and contains the predicted expulsion of the hinge region.

Structure of SRPN2-S358W—The fact that the SRPN2-S358E structure revealed an expelled RCL hinge region prompted us to develop a mutant in which the hinge region insertion could be further stabilized compared with the wild-type protein. Therefore, we generated a SRPN2-S358W mutant, in which Trp^{358} could potentially interact with the hydrophobic residues between strands βA3 and βA5 and thus be buried within the hydrophobic interior of the serpin.

The crystal structure of SRPN2-S358W was determined to a resolution of 1.9 Å (Table 1) and is isomorphous to SRPN2-WT with a single molecule in the asymmetric unit. The root mean square deviation between Cα atoms in SRPN2-S358W and SRPN2-WT was 0.33 Å for 358 residues aligned (Fig. 3*A*). As predicted, the RCL hinge region in SRPN2-S358W adopts a similar conformation compared with SRPN2-WT, buried within the interior of β-sheet A (Fig. 3*B*). The SRPN2-S358W RCL could be modeled to residue Glu^{374}, and Trp^{358} side chain density was clearly defined (Fig. 3*C*). Trp^{358} is located between βA3 and βA5 and is embedded within a hydrophobic pocket composed of Ile^{351} and Ile^{353} on βA5, Phe^{197} on βA3, Phe^{400} on βB5, Ile^{390} on βB4, and Tyr^{251} located between βB2 and βB3 (Fig. 3*D*). Residues Phe^{197}, Phe^{400}, and Tyr^{251} are highly invariant and conserved in ~75% of serpins (62). Subtle conformational changes are observed in multiple residues within this hydrophobic pocket to accommodate the tryptophan side chain. The structure of SRPN2-S358W suggests that Trp^{358} may stabilize the hinge region in an inserted conformation.

Structure of SRPN2-K198C/E359C—Despite the structural data from SRPN2-S358W, it is possible that the region could become intermittently expelled in a dynamic equilibrium as observed previously in ATIII-S380W (40). Therefore, we also

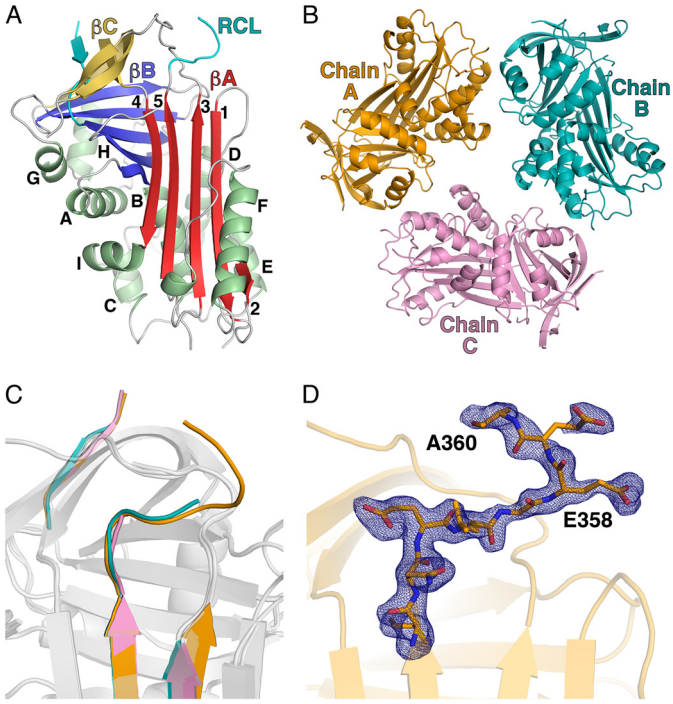

FIGURE 1. **Structure of SRPN2-S358E.** *A*, crystal structure of SRPN2-S358E determined to a resolution of 2.0 Å. β-Sheet A (*red*), β-sheet B (*blue*), β-sheet C (*yellow*), RCL (*cyan*), serpin helices (*A–I*), and βA strands (*1–5*) are identified. *B*, non-crystallographic symmetry trimer of SRPN2-S358E viewed along the 3-fold non-crystallographic symmetry axis showing chain A (*orange*), chain B (*cyan*), and chain C (*pink*). *C*, structural alignment of the RCL, βA3, and βA5 from SRPN2-S358E chain A (*orange*), chain B (*cyan*), and chain C (*pink*). *D*, $F_o - F_c$ omit electron density map (3σ) of the SRPN2-S358E RCL hinge region (Ile^{353}–Ala^{360}).

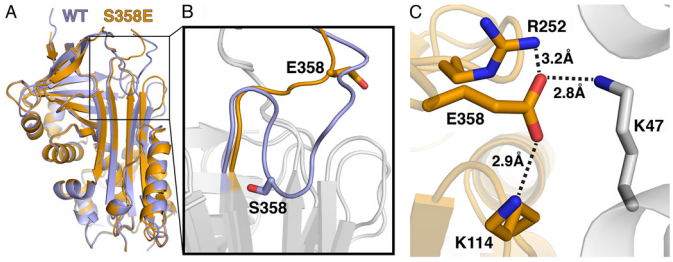

FIGURE 2. **Structural comparison of SRPN2-S358E and SRPN2-WT.** *A*, structural alignment of SRPN2-WT (PDB code 3PZF; *blue*) and chain A of SRPN2-S358E (*orange*). *B*, *close-up* of the alignment of the RCL hinge region from SRPN2-WT (*blue*) and SRPN2-S358E (*orange*) from the *inset* in *A* with Ser^{358} from WT and Glu^{358} from S358E side chains shown. *C*, in the SRPN2-S358E mutant, hydrogen bonds are formed between Glu^{358} and Lys^{114} and Arg^{252} within the protein and with Lys^{47} in chain A of a symmetry-related molecule (*gray*).

created a SRPN2-K198C/E359C mutant in which a disulfide bond is introduced between the hinge region residue Glu^{359} and the adjacent K198C residue located on βA3. Hypothetically, a disulfide bond at this position would strengthen the interaction and maintain the inserted hinge loop region with limited possibility for its expulsion. The introduction of a disulfide bond at this position was used previously for similar purposes in a study of ATIII (42).

The crystal structure of SRPN2-K198C/E359C was determined to a resolution of 2.9 Å (Table 1), containing 12 molecules in the asymmetric unit. The overall conformation of SRPN2-K198C/E359C was very similar to SRPN2-WT with a root mean square deviation of 0.63 Å between Cα atoms for 351 residues aligned (Fig. 4*A*). As predicted, the RCL hinge region in

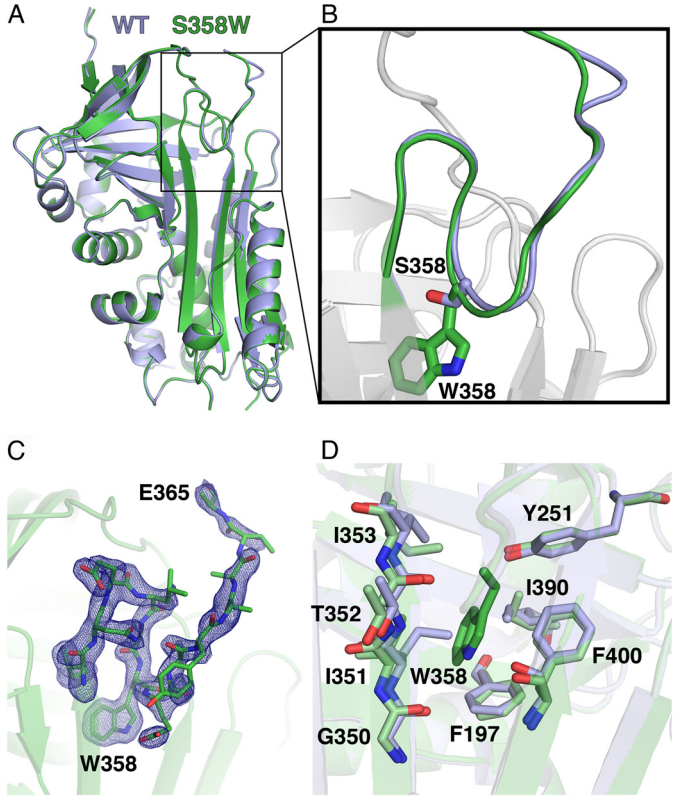

FIGURE 3. **Structure of SRPN2-S358W and comparison with SRPN2-WT.** *A*, crystal structure of SRPN2-S358W determined to a resolution of 1.9 Å (*green*) aligned with SRPN2-WT (PDB code 3PZF; *blue*). *B*, *close-up* of the alignment of the RCL hinge region from SRPN2-WT (*blue*) and SRPN2-S358W (*green*) from the *inset* in *B* with Ser^{358} from WT and Trp^{358} from S358W side chains shown. *C*, $F_o - F_c$ omit electron density map (3σ) of the SRPN2-S358W RCL hinge region (Ile^{353}–Glu^{374}). *D*, in the SRPN2-S358W mutant, Trp^{358} (*green*) inserts into a hydrophobic pocket within the serpin. Shown is the conformation shift of residues in SRPN2-S358W (*green*) surrounding Trp^{358} compared with their position in SRPN2-WT (*blue*).

the SRPN2-K198C/E359C structure is inserted into β-sheet A (Fig. 4*B*). The hinge region of the RCL in the SRPN2-K198C/E359C structure could be modeled up to residue Ala^{360} and shows clear density corresponding to the disulfide bond introduced between Cys^{359} and Cys^{198} (Fig. 4*C*). We further confirmed the presence of the disulfide bond by analyzing SRPN2-WT, SRPN2-K198C, SRPN2-E539C, and SRPN2-K198C/E359C on SDS-PAGE under reducing and nonreducing conditions. All proteins ran at the same size under both conditions except for SRPN2-K198C/E359C, which ran faster under nonreducing compared with reducing conditions, indicating the presence of a disulfide bond (Fig. 4*D*). Therefore, SRPN2-K198C/E359C exists in a native conformation and contains a disulfide bond that stabilizes the partial RCL hinge insertion.

Differences in Thermostability and Structure among the SRPN2 Variants—The SRPN2 variant structures clearly reveal either expulsion or stabilization of the RCL hinge region. To investigate the thermodynamic effects of these mutations, we used differential scanning calorimetry to determine the midpoint transition temperature (T_m) of each variant (Fig. 5*A*). The thermal unfolding transition was absent during repeated scans (data not shown) due to irreversible aggregation of the samples at high temperature. The T_m of SRPN2-WT was 55.9 °C, and a similar T_m of 54.6 °C was determined for SRPN2-S358W. The

expulsion of the hinge region in SRPN2-S358E resulted in a decrease in T_m to 52.9 °C. Whereas Glu^{358} formed new hydrogen bonds with Lys^{114} and Arg^{252}, the network of stabilizing bonds found in the hinge of SRPN2-WT was lost, reducing overall thermodynamic stability. As a consequence, hinge expulsion led to 16 residues in the RCL being left unresolved (residues 361–376), twice as many as were unresolved in the SRPN2-WT structure (residues 367–374). Last, we determined that SRPN2-K198C/E359C had a significant increase in thermostability, with T_m of 60.7 °C. This T_m increase reflects the enhanced protein stability provided by the disulfide bond. Together, these results indicated that differences in the RCL conformation and stabilizing intramolecular interactions between the SRPN2 variants are reflected in their respective thermostabilities.

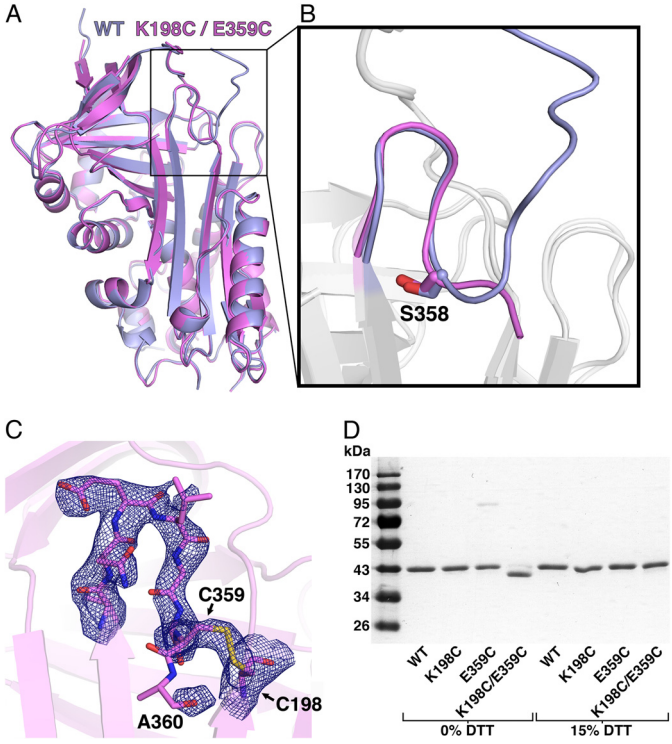

FIGURE 4. **Structure of SRPN2-K198C/E359C and comparison with SRPN2-WT.** *A*, crystal structure of SRPN2-K198C/E359C determined to a resolution of 2.85 Å (*purple*) aligned with SRPN2-WT (PDB code 3PZF; *blue*). *B*, close-up of the alignment of the RCL hinge region from SRPN2-WT (*blue*) and SRPN2-K198C/E359C (*pink*) from the *inset* in *B* with Ser^{358} shown. *C*, $F_o - F_c$ omit electron density map (3σ) of the SRPN2-K198C/E359C RCL hinge region (Ile^{353}–Ala^{360}) contoured at 1.5σ. *D*, Coomassie Blue-stained SDS-polyacrylamide gel showing SRPN2 cysteine mutants in the presence of 0 and 10% DTT. The higher weight molecular band in 0% DTT corresponding to E359C is believed to be due to an intermolecular disulfide bond.

Stoichiometry of Inhibition of SRPN2 Variants—Having established the structure and thermostability of the SRPN2 variants, we determined their ability to form an inhibitory complex with the activated cognate proteinase CLIPB9$_{Xa}$ and the SI of this interaction (Table 2 and Fig. 6). SRPN2-WT forms an SDS-stable complex with CLIPB9$_{Xa}$ with an SI of 1.7 ± 0.1. SRPN2-S358E was also able to inhibit CLIPB9$_{Xa}$ and form an SDS-stable complex with the proteinase with a slightly increased SI of 2.5 ± 0.7, indicating that the expelled hinge mutant is capable of forming an inhibitory complex at a level comparable with SRPN2-WT. Conversely, SRPN2-S358W did

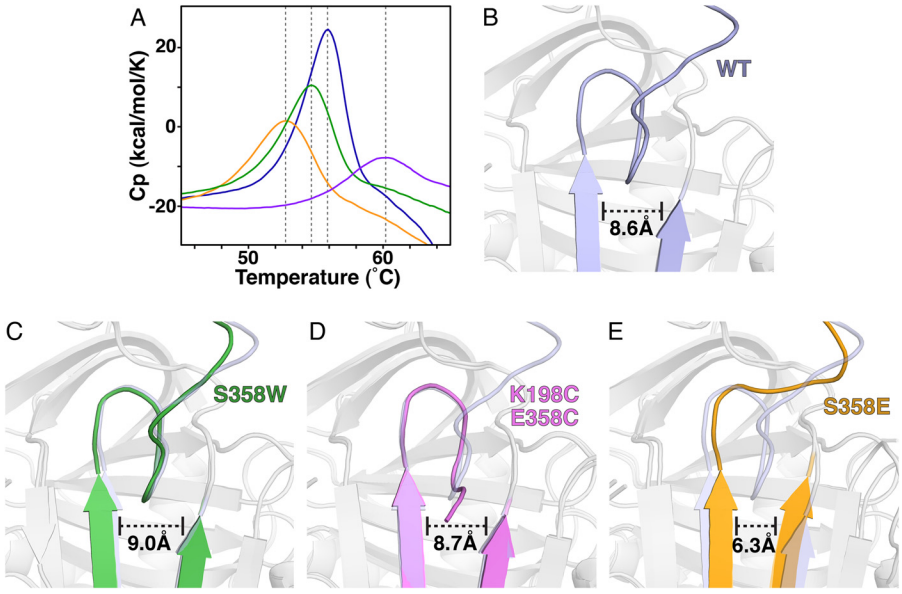

FIGURE 5. **Thermostability of SRPN2 variants and structural changes in β-sheet A.** *A*, differential scanning calorimetry measurements of SRPN2-WT (*blue*), SRPN2-S358W (*green*), SRPN2-K198C/E359C (*purple*), and SRPN2-S358E (*yellow*), indicating the relative mid-point unfolding temperature (T_m; *dotted lines*) as measured by maximum heat capacity (*Cp*). *B*, SRPN2-WT structure with the RCL hinge region and βA3/βA5 (*blue*) shown, including the distance measured between βA3 and βA5. The identical orientation and measurement are shown for SRPN2-S358W (*green*) (*C*), SRPN2-K198C/E359C (*pink*) (*D*), and SRPN2-S358E (*orange*) (*E*).

TABLE 2
***In vitro* inhibition of CLIPB9 by SRPN2 and mutants**

Protein	SI ± S.D.	k_a ± S.D.	k_a × SI ± S.D.
		$M^{-1}\ s^{-1}$	$M^{-1}\ s^{-1}$
SRPN2-WT	1.7 ± 0.1	$(1.5 \pm 0.2) \times 10^3$	$(2.6 \pm 0.2) \times 10^3$
SRPN2-S358E	2.5 ± 0.7	$(2.8 \pm 0.3) \times 10^3$	$(7.1 \pm 0.3) \times 10^3$
SRPN2-S358W	50 ± 12	$(6.1 \pm 0.2) \times 10^1$	$(3.1 \pm 0.1) \times 10^3$
SRPN2-K198C/E359C	20 ± 5	$(2.3 \pm 0.4) \times 10^2$	$(4.6 \pm 0.4) \times 10^3$

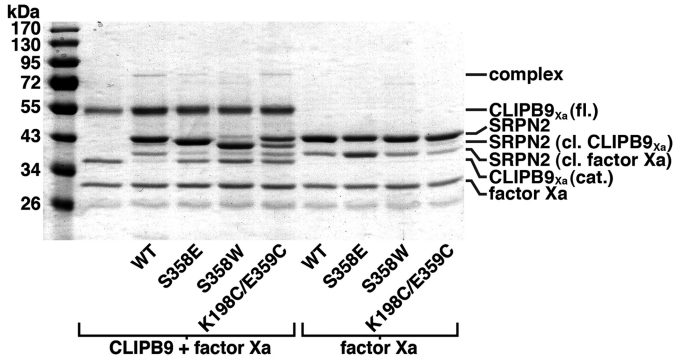

FIGURE 6. **Inhibitory complex formation between CLIPB9 and SRPN2 variants.** SDS-polyacrylamide gel with Coomassie staining after incubation of recombinant SRPN2 variants and $CLIPB9_{Xa}$. $CLIPB9_{Xa}$ must be activated by factor Xa for full catalytic activity. Notable bands are described on the *right*. *fl*, full-length; *cl*, cleaved; *cat*, catalytic domain.

not form an inhibitory complex with CLIPB9, reflected in its significantly increased SI of 50 ± 12 (Table 2 and Fig. 6). However, $CLIPB9_{Xa}$ efficiently degraded SRPN2-S358W, leaving a cleavage product at a size consistent with cleavage at the RCL P1-P1′. Therefore, although SRPN2-S358W cannot inhibit $CLIPB9_{Xa}$, it is efficiently cleaved at the RCL. Surprisingly, SRPN2-K198C/E359C was able to form an inhibitory complex with $CLIPB9_{Xa}$, although the SI was greatly increased to 20 ± 5. SRPN2-K198C/E359C also contained a band in SDS-PAGE consistent with cleavage at the RCL.

Rate of $CLIPB9_{Xa}$ Inhibition by SRPN2 Variants—Having established that the SRPN2 variants, with the exception of SRPN2-S358W, each form an inhibitory complex with $CLIPB9_{Xa}$, we determined the second order rate constants (k_a) of the SPRN2 variants' inhibition against $CLIPB9_{Xa}$ (Table 2). SRPN2-WT was able to inhibit $CLIPB9_{Xa}$ with a k_a of $(1.5 \pm 0.2) \times 10^3\ M^{-1}\ s^{-1}$. Combining this reaction rate with the SI (SI × k_a) provides a measure of total flux down both the substrate and inhibitory pathways of SRPN2-WT with $CLIPB9_{Xa}$ of $(2.6 \pm 0.4) \times 10^3\ M^{-1}\ s^{-1}$. This level of activity is relatively low compared with ATIII, which has inhibitory activity against factor Xa in the $1.0 \times 10^7\ M^{-1}\ s^{-1}$ range when fully activated (40). To determine whether the expelled hinge region increases the inhibitory activity of SRPN2, we measured the k_a of SRPN2-S358E against $CLIPB9_{Xa}$. The k_a of SRPN2-S358E was $(2.8 \pm 0.3) \times 10^3\ M^{-1}\ s^{-1}$, a 1.9-fold increase compared with the k_a of SRPN2-WT. Combining the k_a and SI of SRPN2-S358E, $(7.1 \pm 0.3) \times 10^3\ M^{-1}\ s^{-1}$, indicates that the overall reaction kinetics of SRPN2-S358E are increased nearly 3-fold compared with SRPN2-WT.

We also investigated the second order rate constants of the hinge-inserted SRPN2 variants SRPN2-S358W and SRPN2-K198C/E359C (Table 2). Based on its high SI and inability to form an SDS-stable inhibitory complex, it is not surprising that SRPN2-S358W had a k_a of $(6.1 \pm 0.2) \times 10^1\ M^{-1}\ s^{-1}$. These results confirm that SRPN2-S358W has effectively no inhibitory activity against $CLIPB9_{Xa}$. We determined that the k_a of SRPN2-K198C/E359C was $(2.3 \pm 0.4) \times 10^2\ M^{-1}\ s^{-1}$, which is a 6.7-fold decrease compared with SRPN2-WT. However, the SI of SRPN2-K198C/E359C was significantly increased, indicating that the disulfide bond may hinder this variant's ability to form an inhibitory complex independent of the effect of the inserted hinge region that we are investigating. Combining the SI and k_a for SRPN2-K198C/E359C, $(4.6 \pm 0.4) \times 10^3\ M^{-1}\ s^{-1}$, indicates that this hinge-inserted variant has a similar flux down inhibitor and substrate pathways when interacting with $CLIPB9_{Xa}$, comparable with SRPN2-WT and SRPN2-S358E.

DISCUSSION

SRPN2 is a critical negative regulator of the melanization pathway in *A. gambiae.* The phenotype of SRPN2 depletion from adult female mosquitoes shows accelerated mortality rates and decreased feeding propensity at the time when malaria-infected mosquitoes are able to transmit the parasite to the next human host (11, 12).[4] SRPN2 may therefore be a promising target for small molecule inhibitors to be utilized as late life-acting insecticides for vector control.

The structure of SRPN2-WT revealed a partial insertion of the RCL hinge region into β-sheet A. A very similar partial RCL insertion was linked previously to allosteric activation of ATIII. The ATIII data revealed a model whereby heparin-induced conformational changes resulted in expulsion of the hinge region increasing accessibility of the RCL P1-P1′ and exosites, thereby boosting inhibition of target proteinases. Due to the relative rarity of the inserted hinge region among serpins, we hypothesized that it likewise functions as a regulatory mechanism in SRPN2. To test this hypothesis, we developed SRPN2 mutants with constitutively expelled (SRPN2-S358E) or stabilized (SRPN2-S358W, SRPN2-K198C/E359C) hinge regions, analyzed the structure and thermostability of the variants, and determined the effects of the mutations on inhibition of $CLIPB9_{Xa}$. Our data reveal that a hinge-expelled SRPN2 variant had a limited increase in inhibitory activity against $CLIPB9_{Xa}$ and that stabilization of the inserted hinge region did not affect RCL accessibility. Together, these results strongly suggest that SRPN2 does not follow the ATIII model of allosteric activation by H5.

The hinge-expelled SRPN2-S358E mutant did indeed gain an ~3-fold increase in $CLIPB9_{Xa}$ inhibition, indicating that serpin activity does generally benefit from increased RCL extension and flexibility. However, this increase is much less than the 190-fold increase in the equivalent ATIII-S380E mutant against factor Xa (44). An explanation for the limited advantage in SRPN2 is the possibility that hinge expulsion is achieved by exosite interactions between SRPN2 and CLIPB9 prior to cleavage of the scissile bond. SRPN2-S358E would therefore circumvent this step, gaining 3-fold efficiency. Such exosite interaction would increase the specificity of SRPN2 for CLIPB9, which may be crucial in the physiological context of an open circulatory system. Further structural and mutagenesis studies and inves-

[4] K. Michel, unpublished observations.

tigations into the SRPN2-CLIPB9 interaction will be necessary to test this hypothesis.

An equally parsimonious explanation for the minimal activation of SRPN2-S358E is that accessibility of the P1-P1′ bond is not strongly hindered by the potential hinge insertion. Therefore, CLIPB9 inhibition simply does not require extension of the RCL. We found that $CLIPB9_{Xa}$ cleaves the RCL of both SRPN2-S358W and SRPN2-K198C/E359C, despite their stabilization of the hinge insertion. SRPN2-S358W is unable to form an inhibitory complex with $CLIPB9_{Xa}$, probably due to the bulky P14 residue inhibiting the complete insertion into β-sheet A, which has been reported for other such mutants (63). However, SRPN2-K198C/E359C can form an inhibitory complex with $CLIPB9_{Xa}$, and its increased SI is probably due to effects of the disulfide bond on complete insertion. Furthermore, when SI is taken into consideration, SRPN2-K198C/E359C has an efficiency of interaction with $CLIPB9_{Xa}$ comparable with SRPN2-WT. Therefore, these variants indicate that the partial hinge insertion does not hinder the ability for CLIPB9 to target and cleave the SRPN2 RCL. These data can be interpreted in the context of a recently proposed expansion of the allosteric ATIII activation model (64). This model envisions that lowered activity of hinge-inserted ATIII in the absence of H5 is largely due to repulsive exosite interactions with factors IXa and Xa. These proposed negative exosite interactions are diminished physiologically by conformational changes induced by H5 and presumably are overcome by mutational expulsion of the hinge region as seen in ATIII-S380E. Following this model, efficient cleavage of SRPN2-S358W and SRPN2-K198C/E359C can be explained by the lack of such repulsive exosites in the interaction of SRPN2 with CLIPB9.

Consistent with the idea that RCL accessibility is not a limiting factor of SRPN2 activity, the structural data suggest that the hinge-inserted conformation of SRPN2 provides increased efficiency for complete hinge insertion after P1-P1′ cleavage, thus facilitating inhibitory complex formation. The SRPN2-WT hinge insertion naturally results in a local increase in the distance between βA3 and βA5 that decreases once the hinge is expelled in SRPN2-S358E. Previous studies on ATIII indicated the requirement for coordination of βA strand separation and RCL insertion (44). However, the drastically increased level of RCL cleavage upon hinge expulsion in ATIII would overcome negative effects due to increased βA strand interaction. However, because the SRPN2 RCL is cleaved at similar rates in inserted and expelled forms, the local separation of βA strands may provide an energetic advantage toward rapid insertion. The SRPN2-S358E inhibitory data supports this, with a 1.9-fold increase in SRPN2-S358E k_a (perhaps due to increased RCL accessibility) and a 1.5-fold decrease in SI (due to decreased insertion). The partially inserted hinge region in SRPN2-WT therefore gains an energetic head start toward complete insertion that is not negated by diminished RCL accessibility.

Although the data did not reveal that the inserted hinge in SRPN2 functions as a regulatory mechanism against CLIPB9 inhibition, it is nevertheless conceivable that hinge expulsion is required for inhibition of a yet to be identified proteinase target. Although this possibility is actively pursued, the low level of CLIPB9 inhibition *in vitro* remains intriguing and suggests that a different unidentified mode of SRPN2 regulation may exist *in vivo*. Activation of ATIII against thrombin requires a bridging mechanism mediated by full-length heparin that binds both proteins, in contrast with the allosteric activation mediated by H5 that governs inhibition of factors IXa and Xa (reviewed in Ref. 41). This divergence has been attributed to the poorer suitability of ATIII as a thrombin substrate (44) and the inability of thrombin to utilize exosites critical for contact between ATIII and factors IXa and Xa (41). Molecules that facilitate the initial interaction between thrombin and ATIII are therefore far more likely to increase ATIII activity against thrombin than those that extend the RCL (44). The ATIII-S380E mutation only increases the k_a against thrombin 1.9-fold (44), which correlates intriguingly well with our SRPN2-$CLIPB9_{Xa}$ data. It is tempting to speculate that a bridging mechanism rather than allosteric regulation modulates SRPN2 activity. There are a number of inactive proteinases in the CLIPA family that coordinate protein-protein interactions in different pathways within insect immune systems (65–69). The specific molecular roles of CLIPAs within melanization in mosquitoes await elucidation, and some may indeed regulate SRPN2 activity and thus phenoloxidase activation in *A. gambiae*.

Acknowledgments—We thank Tinea Graves for technical support in the production of mutant SRPN2 expression constructs and the production of recombinant protein. We thank Nurjahan Mehzabeen in the Protein Structure Laboratory for assisting with some of the crystallization experiments.

REFERENCES

1. Sinka, M. E., Bangs, M. J., Manguin, S., Rubio-Palis, Y., Chareonviriyaphap, T., Coetzee, M., Mbogo, C. M., Hemingway, J., Patil, A. P., Temperley, W. H., Gething, P. W., Kabaria, C. W., Burkot, T. R., Harbach, R. E., and Hay, S. I. (2012) A global map of dominant malaria vectors. *Parasit. Vectors* **5,** 69
2. Gething, P. W., Patil, A. P., Smith, D. L., Guerra, C. A., Elyazar, I. R., Johnston, G. L., Tatem, A. J., and Hay, S. I. (2011) A new world malaria map: *Plasmodium falciparum* endemicity in 2010. *Malar. J.* **10,** 378
3. Weiss, D. J., Bhatt, S., Mappin, B., Van Boeckel, T. P., Smith, D. L., Hay, S. I., and Gething, P. W. (2014) Air temperature suitability for Plasmodium falciparum malaria transmission in Africa 2000–2012: a high-resolution spatiotemporal prediction. *Malar. J.* **13,** 171
4. Murray, C. J., Ortblad, K. F., Guinovart, C., Lim, S. S., Wolock, T. M., Roberts, D. A., Dansereau, E. A., Graetz, N., Barber, R. M., Brown, J. C., Wang, H., Duber, H. C., Naghavi, M., Dicker, D., Dandona, L., Salomon, J. A., Heuton, K. R., Foreman, K., Phillips, D. E., Fleming, T. D., Flaxman, A. D., Phillips, B. K., Johnson, E. K., Coggeshall, M. S., Abd-Allah, F., Abera, S. F., Abraham, J. P., Abubakar, I., Abu-Raddad, L. J., Abu-Rmeileh, N. M., Achoki, T., Adeyemo, A. O., Adou, A. K., Adsuar, J. C., Agardh, E. E., Akena, D., Al Kahbouri, M. J., Alasfoor, D., Albittar, M. I., Alcalá-Cerra, G., Alegretti, M. A., Alemu, Z. A., Alfonso-Cristancho, R., Alhabib, S., Ali, R., Alla, F., Allen, P. J., Alsharif, U., Alvarez, E., Alvis-Guzman, N., Amankwaa, A. A., Amare, A. T., Amini, H., Ammar, W., Anderson, B. O., Antonio, C. A., Anwari, P., Arnlov, J., Arsenijevic, V. S., Artaman, A., Asghar, R. J., Assadi, R., Atkins, L. S., Badawi, A., Balakrishnan, K., Banerjee, A., Basu, S., Beardsley, J., Bekele, T., Bell, M. L., Bernabe, E., Beyene, T. J., Bhala, N., Bhalla, A., Bhutta, Z. A., Abdulhak, A. B., Binagwaho, A., Blore, J. D., Basara, B. B., Bose, D., Brainin, M., Breitborde, N., Castaneda-Orjuela, C. A., Catala-Lopez, F., Chadha, V. K., Chang, J. C., Chiang, P. P., Chuang, T. W., Colomar, M., Cooper, L. T., Cooper, C., Courville, K. J., Cowie, B. C., Criqui, M. H., Dandona, R., Dayama, A., De Leo, D., Degenhardt, L., Del Pozo-Cruz, B., Deribe, K., Des Jarlais, D. C., Dessalegn, M., Dharmaratne, S. D., Dilmen, U., Ding, E. L., Driscoll, T. R., Durrani, A. M.,

Ellenbogen, R. G., Ermakov, S. P., Esteghamati, A., Faraon, E. J., Farzadfar, F., Fereshtehnejad, S. M., Fijabi, D. O., Forouzanfar, M. H., Fra Paleo, U., Gaffikin, L., Gamkrelidze, A., Gankpe, F. G., Geleijnse, J. M., Gessner, B. D., Gibney, K. B., Ginawi, I. A., Glaser, E. L., Gona, P., Goto, A., Gouda, H. N., Gugnani, H. C., Gupta, R., Hafezi-Nejad, N., Hamadeh, R. R., Hammami, M., Hankey, G. J., Harb, H. L., Haro, J. M., Havmoeller, R., Hay, S. I., Hedayati, M. T., Pi, I. B., Hoek, H. W., Hornberger, J. C., Hosgood, H. D., Hotez, P. J., Hoy, D. G., Huang, J. J., Iburg, K. M., Idrisov, B. T., Innos, K., Jacobsen, K. H., Jeemon, P., Jensen, P. N., Jha, V., Jiang, G., Jonas, J. B., Juel, K., Kan, H., Kankindi, I., Karam, N. E., Karch, A., Karema, C. K., Kaul, A., Kawakami, N., Kazi, D. S., Kemp, A. H., Kengne, A. P., Keren, A., Kereselidze, M., Khader, Y. S., Khalifa, S. E., Khan, E. A., Khang, Y. H., Khonelidze, I., Kinfu, Y., Kinge, J. M., Knibbs, L., Kokubo, Y., Kosen, S., Defo, B. K., Kulkarni, V. S., Kulkarni, C., Kumar, K., Kumar, R. B., Kumar, G. A., Kwan, G. F., Lai, T., Balaji, A. L., Lam, H., Lan, Q., Lansingh, V. C., Larson, H. J., Larsson, A., Lee, J. T., Leigh, J., Leinsalu, M., Leung, R., Li, Y., De Lima, G. M., Lin, H. H., Lipshultz, S. E., Liu, S., Liu, Y., Lloyd, B. K., Lotufo, P. A., Machado, V. M., Maclachlan, J. H., Magis-Rodriguez, C., Majdan, M., Mapoma, C. C., Marcenes, W., Marzan, M. B., Masci, J. R., Mashal, M. T., Mason-Jones, A. J., Mayosi, B. M., Mazorodze, T. T., McKay, A. C., Meaney, P. A., Mehndiratta, M. M., Mejia-Rodriguez, F., Melaku, Y. A., Memish, Z. A., Mendoza, W., Miller, T. R., Mills, E. J., Mohammad, K. A., Mokdad, A. H., Mola, G. L., Monasta, L., Montico, M., Moore, A. R., Mori, R., Moturi, W. N., Mukaigawara, M., Murthy, K. S., Naheed, A., Naidoo, K. S., Naldi, L., Nangia, V., Narayan, K. M., Nash, D., Nejjari, C., Nelson, R. G., Neupane, S. P., Newton, C. R., Ng, M., Nisar, M. I., Nolte, S., Norheim, O. F., Nowaseb, V., Nyakarahuka, L., Oh, I. H., Ohkubo, T., Olusanya, B. O., Omer, S. B., Opio, J. N., Orisakwe, O. E., Pandian, J. D., Papachristou, C., Caicedo, A. J., Patten, S. B., Paul, V. K., Pavlin, B. I., Pearce, N., Pereira, D. M., Pervaiz, A., Pesudovs, K., Petzold, M., Pourmalek, F., Qato, D., Quezada, A. D., Quistberg, D. A., Rafay, A., Rahimi, K., Rahimi-Movaghar, V., Ur Rahman, S., Raju, M., Rana, S. M., Razavi, H., Reilly, R. Q., Remuzzi, G., Richardus, J. H., Ronfani, L., Roy, N., Sabin, N., Saeedi, M. Y., Sahraian, M. A., Samonte, G. M., Sawhney, M., Schneider, I. J., Schwebel, D. C., Seedat, S., Sepanlou, S. G., Servan-Mori, E. E., Sheikhbahaei, S., Shibuya, K., Shin, H. H., Shiue, I., Shivakoti, R., Sigfusdottir, I. D., Silberberg, D. H., Silva, A. P., Simard, E. P., Singh, J. A., Skirbekk, V., Sliwa, K., Soneji, S., Soshnikov, S. S., Sreeramareddy, C. T., Stathopoulou, V. K., Stroumpoulis, K., Swaminathan, S., Sykes, B. L., Tabb, K. M., Talongwa, R. T., Tenkorang, E. Y., Terkawi, A. S., Thomson, A. J., Thorne-Lyman, A. L., Towbin, J. A., Traebert, J., Tran, B. X., Dimbuene, Z. T., Tsilimbaris, M., Uchendu, U. S., Ukwaja, K. N., Uzun, S. B., Vallely, A. J., Vasankari, T. J., Venketasubramanian, N., Violante, F. S., Vlassov, V. V., Vollset, S. E., Waller, S., Wallin, M. T., Wang, L., Wang, X., Wang, Y., Weichenthal, S., Weiderpass, E., Weintraub, R. G., Westerman, R., White, R. A., Wilkinson, J. D., Williams, T. N., Woldeyohannes, S. M., Wong, J. Q., Xu, G., Yang, Y. C., Yano, Y., Yentur, G. K., Yip, P., Yonemoto, N., Yoon, S. J., Younis, M., Yu, C., Jin, K. Y., El Sayed Zaki, M., Zhao, Y., Zheng, Y., Zhou, M., Zhu, J., Zou, X. N., Lopez, A. D., and Vos, T. (2014) Global, regional, and national incidence and mortality for HIV, tuberculosis, and malaria during 1990–2013: a systematic analysis for the Global Burden of Disease Study 2013. *Lancet* **384,** 1005–1070

5. Enayati, A., and Hemingway, J. (2010) Malaria management: past, present, and future. *Annu. Rev. Entomol.* **55,** 569–591
6. Karunamoorthi, K. (2014) Malaria vaccine: a future hope to curtail the global malaria burden. *Int. J. Prev. Med.* **5,** 529–538
7. Silva, A. P., Santos, J. M., and Martins, A. J. (2014) Mutations in the voltage-gated sodium channel gene of anophelines and their association with resistance to pyrethroids: a review. *Parasit. Vectors* **7,** 450
8. Knox, T. B., Juma, E. O., Ochomo, E. O., Pates Jamet, H., Ndungo, L., Chege, P., Bayoh, N. M., N'Guessan, R., Christian, R. N., Hunt, R. H., and Coetzee, M. (2014) An online tool for mapping insecticide resistance in major *Anopheles* vectors of human malaria parasites and review of resistance status for the Afrotropical region. *Parasit. Vectors* **7,** 76
9. Read, A. F., Lynch, P. A., and Thomas, M. B. (2009) How to make evolution-proof insecticides for malaria control. *PLoS Biol.* **7,** e1000058
10. Koella, J. C., Lorenz, L., and Bargielowski, I. (2009) Microsporidians as evolution-proof agents of malaria control? *Adv. Parasitol.* **68,** 315–327
11. Michel, K., Budd, A., Pinto, S., Gibson, T. J., and Kafatos, F. C. (2005) *Anopheles gambiae* SRPN2 facilitates midgut invasion by the malaria parasite *Plasmodium berghei*. *EMBO Rep.* **6,** 891–897
12. An, C., Budd, A., Kanost, M. R., and Michel, K. (2011) Characterization of a regulatory unit that controls melanization and affects longevity of mosquitoes. *Cell. Mol. Life Sci.* **68,** 1929–1939
13. Yassine, H., and Osta, M. A. (2010) *Anopheles gambiae* innate immunity. *Cell Microbiol.* **12,** 1–9
14. Hillyer, J. F. (2010) Mosquito immunity. *Adv. Exp. Med. Biol.* **708,** 218–238
15. Crompton, P. D., Moebius, J., Portugal, S., Waisberg, M., Hart, G., Garver, L. S., Miller, L. H., Barillas-Mury, C., and Pierce, S. K. (2014) Malaria immunity in man and mosquito: insights into unsolved mysteries of a deadly infectious disease. *Annu. Rev. Immunol.* **32,** 157–187
16. Christensen, B. M., Li, J., Chen, C. C., and Nappi, A. J. (2005) Melanization immune responses in mosquito vectors. *Trends Parasitol.* **21,** 192–199
17. Tang, H., Kambris, Z., Lemaitre, B., and Hashimoto, C. (2006) Two proteases defining a melanization cascade in the immune system of *Drosophila*. *J. Biol. Chem.* **281,** 28097–28104
18. Satoh, D., Horii, A., Ochiai, M., and Ashida, M. (1999) Prophenoloxidase-activating enzyme of the silkworm, *Bombyx mori*. Purification, characterization, and cDNA cloning. *J. Biol. Chem.* **274,** 7441–7453
19. Kan, H., Kim, C. H., Kwon, H. M., Park, J. W., Roh, K. B., Lee, H., Park, B. J., Zhang, R., Zhang, J., Söderhäll, K., Ha, N. C., and Lee, B. L. (2008) Molecular control of phenoloxidase-induced melanin synthesis in an insect. *J. Biol. Chem.* **283,** 25316–25323
20. Cerenius, L., Kawabata, S., Lee, B. L., Nonaka, M., and Söderhäll, K. (2010) Proteolytic cascades and their involvement in invertebrate immunity. *Trends Biochem. Sci.* **35,** 575–583
21. Volz, J., Osta, M. A., Kafatos, F. C., and Müller, H. M. (2005) The roles of two clip domain serine proteases in innate immune responses of the malaria vector *Anopheles gambiae*. *J. Biol. Chem.* **280,** 40161–40168
22. Jiang, H., Wang, Y., Yu, X. Q., Zhu, Y., and Kanost, M. (2003) Prophenoloxidase-activating proteinase-3 (PAP-3) from *Manduca sexta* hemolymph: a clip-domain serine proteinase regulated by serpin-1J and serine proteinase homologs. *Insect Biochem. Mol. Biol.* **33,** 1049–1060
23. Jiang, H., Wang, Y., and Kanost, M. R. (1998) Pro-phenol oxidase activating proteinase from an insect, Manduca sexta: a bacteria-inducible protein similar to *Drosophila easter*. *Proc. Natl. Acad. Sci. U.S.A.* **95,** 12220–12225
24. Lu, A., Zhang, Q., Zhang, J., Yang, B., Wu, K., Xie, W., Luan, Y. X., and Ling, E. (2014) Insect prophenoloxidase: the view beyond immunity. *Front. Physiol.* **5,** 252
25. Ratcliffe, N. A., Leonard, C., and Rowley, A. F. (1984) Prophenoloxidase activation: nonself recognition and cell cooperation in insect immunity. *Science* **226,** 557–559
26. Gulley, M. M., Zhang, X., and Michel, K. (2013) The roles of serpins in mosquito immunology and physiology. *J. Insect Physiol.* **59,** 138–147
27. Olson, S. T., and Gettins, P. G. (2011) Regulation of proteases by protein inhibitors of the serpin superfamily. *Prog. Mol. Biol. Transl. Sci.* **99,** 185–240
28. Gettins, P. G. (2002) Serpin structure, mechanism, and function. *Chem. Rev.* **102,** 4751–4804
29. Dunstone, M. A., and Whisstock, J. C. (2011) Crystallography of serpins and serpin complexes. *Methods Enzymol.* **501,** 63–87
30. Huntington, J. A., Read, R. J., and Carrell, R. W. (2000) Structure of a serpin-protease complex shows inhibition by deformation. *Nature* **407,** 923–926
31. An, C., Lovell, S., Kanost, M. R., Battaile, K. P., and Michel, K. (2011) Crystal structure of native *Anopheles gambiae* serpin-2, a negative regulator of melanization in mosquitoes. *Proteins* **79,** 1999–2003
32. McCoy, A. J., Pei, X. Y., Skinner, R., Abrahams, J. P., and Carrell, R. W. (2003) Structure of β-antithrombin and the effect of glycosylation on antithrombin's heparin affinity and activity. *J. Mol. Biol.* **326,** 823–833
33. Schreuder, H. A., de Boer, B., Dijkema, R., Mulders, J., Theunissen, H. J., Grootenhuis, P. D., and Hol, W. G. (1994) The intact and cleaved human antithrombin III complex as a model for serpin-proteinase interactions. *Nat. Struct. Biol.* **1,** 48–54
34. Baglin, T. P., Carrell, R. W., Church, F. C., Esmon, C. T., and Huntington,

J. A. (2002) Crystal structures of native and thrombin-complexed heparin cofactor II reveal a multistep allosteric mechanism. *Proc. Natl. Acad. Sci. U.S.A.* **99,** 11079–11084
35. Horvath, A. J., Irving, J. A., Rossjohn, J., Law, R. H., Bottomley, S. P., Quinsey, N. S., Pike, R. N., Coughlin, P. B., and Whisstock, J. C. (2005) The murine orthologue of human antichymotrypsin: a structural paradigm for clade A3 serpins. *J. Biol. Chem.* **280,** 43168–43178
36. Park, S. H., Jiang, R., Piao, S., Zhang, B., Kim, E. H., Kwon, H. M., Jin, X. L., Lee, B. L., and Ha, N. C. (2011) Structural and functional characterization of a highly specific serpin in the insect innate immunity. *J. Biol. Chem.* **286,** 1567–1575
37. Jin, L., Abrahams, J. P., Skinner, R., Petitou, M., Pike, R. N., and Carrell, R. W. (1997) The anticoagulant activation of antithrombin by heparin. *Proc. Natl. Acad. Sci. U.S.A.* **94,** 14683–14688
38. Izaguirre, G., and Olson, S. T. (2006) Residues Tyr^{253} and Glu^{255} in strand 3 of β-sheet C of antithrombin are key determinants of an exosite made accessible by heparin activation to promote rapid inhibition of factors Xa and IXa. *J. Biol. Chem.* **281,** 13424–13432
39. Johnson, D. J., Li, W., Adams, T. E., and Huntington, J. A. (2006) Antithrombin-S195A factor Xa-heparin structure reveals the allosteric mechanism of antithrombin activation. *EMBO J.* **25,** 2029–2037
40. Huntington, J. A., Olson, S. T., Fan, B., and Gettins, P. G. (1996) Mechanism of heparin activation of antithrombin: evidence for reactive center loop preinsertion with expulsion upon heparin binding. *Biochemistry* **35,** 8495–8503
41. Olson, S. T., Richard, B., Izaguirre, G., Schedin-Weiss, S., and Gettins, P. G. (2010) Molecular mechanisms of antithrombin-heparin regulation of blood clotting proteinases: a paradigm for understanding proteinase regulation by serpin family protein proteinase inhibitors. *Biochimie* **92,** 1587–1596
42. Langdown, J., Johnson, D. J., Baglin, T. P., and Huntington, J. A. (2004) Allosteric activation of antithrombin critically depends upon hinge region extension. *J. Biol. Chem.* **279,** 47288–47297
43. Huntington, J. A., and Gettins, P. G. (1998) Conformational conversion of antithrombin to a fully activated substrate of factor Xa without need for heparin. *Biochemistry* **37,** 3272–3277
44. Futamura, A., and Gettins, P. G. (2000) Serine 380 (P14) → glutamate mutation activates antithrombin as an inhibitor of factor Xa. *J. Biol. Chem.* **275,** 4092–4098
45. Jiang, H., Mulnix, A. B., and Kanost, M. R. (1995) Expression and characterization of recombinant *Manduca sexta* serpin-1B and site-directed mutants that change its inhibitory selectivity. *Insect Biochem. Mol. Biol.* **25,** 1093–1100
46. Kabsch, W. (1988) Automatic indexing of rotation diffraction patterns. *J. Appl. Crystallogr.* **21,** 67–72
47. Evans, P. R. (2011) An introduction to data reduction: space-group determination, scaling and intensity statistics. *Acta Crystallogr. D. Biol. Crystallogr.* **67,** 282–292
48. McCoy, A. J., Grosse-Kunstleve, R. W., Adams, P. D., Winn, M. D., Storoni, L. C., and Read, R. J. (2007) Phaser crystallographic software. *J. Appl. Crystallogr.* **40,** 658–674
49. Adams, P. D., Afonine, P. V., Bunkóczi, G., Chen, V. B., Davis, I. W., Echols, N., Headd, J. J., Hung, L. W., Kapral, G. J., Grosse-Kunstleve, R. W., McCoy, A. J., Moriarty, N. W., Oeffner, R., Read, R. J., Richardson, D. C., Richardson, J. S., Terwilliger, T. C., and Zwart, P. H. (2010) PHENIX: a comprehensive Python-based system for macromolecular structure solution. *Acta Crystallogr. D Biol. Crystallogr.* **66,** 213–221
50. Vagin, A., and Teplyakov, A. (2010) Molecular replacement with MOLREP. *Acta Crystallogr. D* **66,** 22–25
51. Emsley, P., Lohkamp, B., Scott, W. G., and Cowtan, K. (2010) Features and development of Coot. *Acta Crystallogr. D Biol. Crystallogr.* **66,** 486–501
52. Painter, J., and Merritt, E. A. (2006) Optimal description of a protein structure in terms of multiple groups undergoing TLS motion. *Acta Crystallogr. D Biol. Crystallogr.* **62,** 439–450
53. Chen, V. B., Arendall, W. B., 3rd, Headd, J. J., Keedy, D. A., Immormino, R. M., Kapral, G. J., Murray, L. W., Richardson, J. S., and Richardson, D. C. (2010) MolProbity: all-atom structure validation for macromolecular crystallography. *Acta Crystallogr. D Biol. Crystallogr.* **66,** 12–21
54. DeLano, W. L. (2010) *The PyMOL Molecular Graphics System*, version 1.3, Schrödinger, LLC, New York
55. Potterton, L., McNicholas, S., Krissinel, E., Gruber, J., Cowtan, K., Emsley, P., Murshudov, G. N., Cohen, S., Perrakis, A., and Noble, M. (2004) Developments in the CCP4 molecular-graphics project. *Acta Crystallogr. D Biol. Crystallogr.* **60,** 2288–2294
56. Wang, J., Kamtekar, S., Berman, A. J., and Steitz, T. A. (2005) Correction of x-ray intensities from single crystals containing lattice-translocation defects. *Acta Crystallogr. D Biol. Crystallogr.* **61,** 67–74
57. Lebedev, A. A., and Isupov, M. N. (2014) Space-group and origin ambiguity in macromolecular structures with pseudo-symmetry and its treatment with the program Zanuda. *Acta Crystallogr. D. Biol. Crystallogr.* **70,** 2430–2443
58. Murshudov, G. N., Vagin, A. A., and Dodson, E. J. (1997) Refinement of macromolecular structures by the maximum-likelihood method. *Acta Crystallogr. D. Biol. Crystallogr.* **53,** 240–255
59. Schick, C., Kamachi, Y., Bartuski, A. J., Cataltepe, S., Schechter, N. M., Pemberton, P. A., and Silverman, G. A. (1997) Squamous cell carcinoma antigen 2 is a novel serpin that inhibits the chymotrypsin-like proteinases cathepsin G and mast cell chymase. *J. Biol. Chem.* **272,** 1849–1855
60. Van Walderveen, M. C., Berry, L. R., and Chan, A. K. (2010) Effect of covalent antithrombin-heparin on activated protein C inactivation by protein C inhibitor. *J. Biochem.* **148,** 255–260
61. Krissinel, E., and Henrick, K. (2004) Secondary-structure matching (SSM), a new tool for fast protein structure alignment in three dimensions. *Acta Crystallogr. D Biol. Crystallogr.* **60,** 2256–2268
62. Irving, J. A., Pike, R. N., Lesk, A. M., and Whisstock, J. C. (2000) Phylogeny of the serpin superfamily: implications of patterns of amino acid conservation for structure and function. *Genome Res.* **10,** 1845–1864
63. Hood, D. B., Huntington, J. A., and Gettins, P. G. (1994) α1-Proteinase inhibitor variant T345R: influence of P14 residue on substrate and inhibitory pathways. *Biochemistry* **33,** 8538–8547
64. Dementiev, A., Swanson, R., Roth, R., Isetti, G., Izaguirre, G., Olson, S. T., and Gettins, P. G. (2013) The allosteric mechanism of activation of antithrombin as an inhibitor of factor IXa and factor Xa: heparin-independent full activation through mutations adjacent to helix D. *J. Biol. Chem.* **288,** 33611–33619
65. Felföldi, G., Eleftherianos, I., Ffrench-Constant, R. H., and Venekei, I. (2011) A serine proteinase homologue, SPH-3, plays a central role in insect immunity. *J. Immunol.* **186,** 4828–4834
66. Gupta, S., Wang, Y., and Jiang, H. (2005) Manduca sexta prophenoloxidase (proPO) activation requires proPO-activating proteinase (PAP) and serine proteinase homologs (SPHs) simultaneously. *Insect Biochem. Mol. Biol.* **35,** 241–248
67. Povelones, M., Bhagavatula, L., Yassine, H., Tan, L. A., Upton, L. M., Osta, M. A., and Christophides, G. K. (2013) The CLIP-domain serine protease homolog SPCLIP1 regulates complement recruitment to microbial surfaces in the malaria mosquito *Anopheles gambiae*. *PLoS Pathog.* **9,** e1003623
68. Volz, J., Müller, H. M., Zdanowicz, A., Kafatos, F. C., and Osta, M. A. (2006) A genetic module regulates the melanization response of *Anopheles* to *Plasmodium*. *Cell Microbiol.* **8,** 1392–1405
69. Yu, X. Q., Jiang, H., Wang, Y., and Kanost, M. R. (2003) Nonproteolytic serine proteinase homologs are involved in prophenoloxidase activation in the tobacco hornworm, *Manduca sexta*. *Insect Biochem. Mol. Biol.* **33,** 197–208
70. Evans, P. (2006) Scaling and assessment of data quality. *Acta Crystallogr. D Biol. Crystallogr.* **62,** 72–82
71. Diederichs, K., and Karplus, P. A. (1997) Improved *R*-factors for diffraction data analysis in macromolecular crystallography. *Nat. Struct. Biol.* **4,** 269–275
72. Weiss, M. S. (2001) Global indicators of x-ray data quality. *J. Appl. Crystallogr.* **34,** 130–135
73. Karplus, P. A., and Diederichs, K. (2012) Linking crystallographic model and data quality. *Science* **336,** 1030–1033
74. Evans, P. (2012) Biochemistry: resolving some old problems in protein crystallography. *Science* **336,** 986–987
75. Chiu, J., March, P. E., Lee, R., and Tillett, D. (2004) Site-directed, ligase-independent mutagenesis (SLIM): a single-tube methodology approaching 100% efficiency in 4 h. *Nucleic Acids Res.* **32,** e174